Journal Pre-proofs

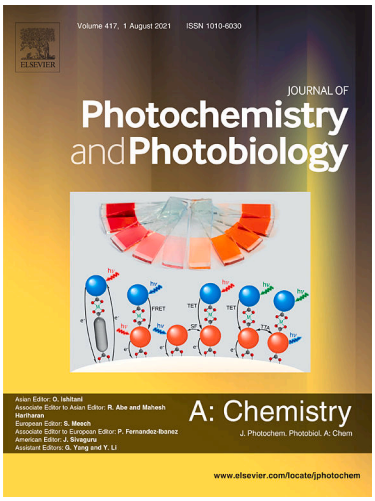

Ce_2O_3 and TiO_2 p-n heterojunction for enhanced degradation of p-nitrophenol under visible light

Antoine Farcy, Maxine Mathy, Louise Lejeune, Pierre Eloy, Sophie Hermans, Patrick Drogui, Julien G. Mahy

PII: S1010-6030(25)00024-3
DOI: https://doi.org/10.1016/j.jphotochem.2025.116284
Reference: JPC 116284

To appear in: *Journal of Photochemistry & Photobiology, A: Chemistry*

Received Date: 21 October 2024
Revised Date: 20 December 2024
Accepted Date: 20 January 2025

Please cite this article as: A. Farcy, M. Mathy, L. Lejeune, P. Eloy, S. Hermans, P. Drogui, J.G. Mahy, Ce_2O_3 and TiO_2 p-n heterojunction for enhanced degradation of p-nitrophenol under visible light, *Journal of Photochemistry & Photobiology, A: Chemistry* (2025), doi: https://doi.org/10.1016/j.jphotochem.2025.116284

Ce_2O_3 and TiO_2 p-n heterojunction for enhanced degradation of p-nitrophenol under visible light

Antoine Farcy[1], Maxine Mathy[1], Louise Lejeune[2], Pierre Eloy[2], Sophie Hermans[2], Patrick Drogui[3], Julien G. Mahy[1,3]*

[1] Department of Chemical Engineering – Nanomaterials, Catalysis & Electrochemistry, University of Liège, Liège, Belgium

[2] Institute of Condensed Matter and Nanosciences - Molecular Chemistry, Materials and Catalysis (IMCN/MOST), Université catholique de Louvain, Place Louis Pasteur 1, Box L4.01.03, 1348 Louvain-La-Neuve, Belgium

[3] Centre INRS – Eau, Terre, Environnement (INRS-ETE), Québec City, Canada

*Corresponding author: Julien G. Mahy; email: julien.mahy@uliege.be; address: Allée du Six Août 11, 4000 Liège, Belgium

Abstract

A sol-gel method is used to synthesize TiO_2, using few organic products. In order to increase the photocatalytic activity in the near visible range (395 nm), cerium is used as a dopant at various concentrations ranging from 0.03 mol% to 4.40 mol%. The addition of cerium leads to the formation of p-n heterojunctions between Ce_2O_3 and TiO_2, multiplying by 2 (under UV-visible light) or 2.6 (under visible light) the photocatalytic efficiency of the composite material with the best dopant amount, i.e. 0.06 mol% of cerium. X-ray diffraction showed the formation of TiO_2 in its anatase form, while nitrogen adsorption/desorption isotherms showed changes in specific surface area as a function of the percentage of cerium added. The presence of cerium (III) in the sample is confirmed by XPS and the amount is determined quantitatively by ICP. DRUS analysis highlights the difference in bandgap caused by the Ce_2O_3 incorporated into the sample. In order to compare the different photocatalysts obtained, the degradation of p-nitrophenol is tested in their presence in water under UV light as well as a wavelength close to the visible range, i.e. 395 nm. Finally, based on the results obtained by electron paramagnetic resonance, a photoactivation mechanism of the mixed oxide is proposed.

Keywords

Photocatalysis, Titanium dioxide, doping, pollutant degradation, water treatment

1. Introduction

Water is an essential resource for life, and its depollution is an increasing necessity, in line with the growing industrial activity of today's societies. Without water quality control, citizens risk major health problems. Traditional methods of water depollution include various chemical, biological or physical processes, each with their advantages and disadvantages [1–3]. For instance, chlorination, which involves adding chlorine to water, can treat a wide range of pollutants, but has the disadvantage of producing harmful by-products [4]. Moreover, these types of methods are ineffective when it comes to degrading recalcitrant organic pollutants in low concentrations [5].

These past decades, advanced oxidation processes (AOPs) have attracted increasing attention for degrading organic pollutants in water [6]. These processes consist in treatments performed at room temperature and atmospheric pressure and are based on the *in situ* generation of a powerful oxidizing agent, such as •OH, at a sufficient concentration to efficiently decontaminate water [6]. Among AOPs, various methods are established for the sustainable removal of a large range of organic pollutants such as the Fenton reaction [7] or homogeneous/heterogeneous photocatalysis [8,9]. The latter includes several non-negligeable advantages such as ease of catalyst production, low costs, and ease of process implementation. Well-known photocatalysts include TiO_2, which has a bandgap of ~3 eV, is easy to synthesize and has low affinity for water, so there is no propensity for leaching of Ti^{4+} ions into the water, which means the catalyst lasts longer when used in an aqueous medium [10]. However, the use of TiO_2 as photocatalyst has two main limitations: (i) the fast charge recombination and (ii) the high band gap value requiring UV-A light for activation.

Among the existing techniques to overcome these limitations, doping is very widespread: by replacing ions in the TiO_2 matrix, elements of other kinds are incorporated to create intermediate energy levels in the bandgap in order to minimize the energy required to generate radicals [8]. Heterojunctions are a type of doping used to create interfaces between the TiO_2 and another semiconductor by introducing new phase in the solid sample [11]. Previously, some studies have shown the possibility to combine TiO_2 with ZnO [12], ZrO_2 [13], SnO_2 [14] or Ce_2O_3 [15]. Among these oxides, Ce_2O_3 presents particularly interesting properties to form heterojunction with TiO_2 as its absorption in visible range [15,16], its easy reduction/oxidation between Ce^{3+} and Ce^{4+} which could contribute to decrease the electron-hole pairs recombination and improve the photocatalytic reaction [16,17], and its ability to transport oxygen ions [18]. Moreover, the unique catalytic properties of Ce_2O_3 by itself make it a good candidate to increase TiO_2 photoactivity [15,19]. It is also a dopant of choice for TiO_2 because it is the most abundant of the lanthanides [20] and it is not-toxic [21].

The aim of this study will be to examine the effect of adding cerium in different quantities on the ability to activate the TiO_2 photocatalyst in the visible range and to increase its activity in UV region. Among the variety of existing techniques for synthesizing this catalyst, our focus will be on the sol-gel method [22], which offers a number of advantages, including the ability to work at ambient pressure and low temperature. This new TiO_2 synthesis process has the advantage of using water as the solvent limiting the use of organic reagents and producing the material at ambient temperature to make it easily up scalable. The material will be characterized by X-Ray Diffraction (XRD), which will allow us to identify the phases obtained after synthesis of the material. The specific surface area, determined from nitrogen adsorption/desorption isotherms, will give an indication on how cerium dosage influences the textural properties. Inductive Coupled Plasma (ICP) enables the exact quantity of cerium present to be determined, which will be supported by Energy Dispersive X-ray spectroscopy (EDX). X-ray photoelectron spectroscopy (XPS) will provide information on the cerium oxidation state and energy bond. Finally, Diffuse Reflectance UV-vis Spectroscopy (DRUS) and electron paramagnetic resonance (EPR) will provide information on how the bandgap is influenced by the amount of cerium.

Photocatalytic activity will be estimated using a model pollutant: p-nitrophenol (PNP) [23]. Finally, in the light of all the previous results and according to certain hypotheses, a photoactivation mechanism of the heterojunction will be proposed.

2. Materials and Methods

2.1. Pure TiO_2 synthesis

Titanium (IV) tetraisopropoxide (TTIP, > 97%, Sigma-Aldrich), sulfuric acid (H_2SO_4, 95%, Merck), and distilled water are used as starting materials.

Firstly, 250 mL of distilled water is acidified with H_2SO_4 to reach a pH of 1. Then, 35 ml of TTIP is added to the water under stirring at ambient temperature. After 4 h, a white slurry is obtained. The slurry is centrifuged and washed twice with distilled water, then dried at 100 °C overnight. The white powder is then calcined 2 h at 500 °C. The pure sample is denoted *pure TiO_2*.

2.2. Ce-doped TiO_2 synthesis

Ce-doped samples are synthesized using Cerium (IV) sulfate ($Ce(SO_4)_2$, Sigma Aldrich) as cerium precursor. The synthesis steps are identical to pure TiO_2 synthesis ones, but the Ce precursor is added to the water after acidification. After reaction at ambient temperature for 4 h, yellowish slurries are obtained. The slurries are also centrifuged and washed twice with distilled water, then dried at 100 °C overnight. The yellow powders are then calcined 2 h at 500 °C.

Seven Ce-doping ratios are studied: 0.03, 0.06, 0.3, 0.35, 0.95, 2.30 and 4.40 mol%. Samples are denoted as TiO_2/Ce_X where X corresponds to the Ce dopant amount. For example, for $TiO_2/Ce_{2.3}$, 0.93 g of Cerium (IV) sulfate was used in the synthesis.

2.3. Material characterizations

The actual amount of cerium in the Ce-doped TiO_2 samples is determined by inductively coupled plasma–atomic emission spectroscopy (ICP–AES), equipped with an ICAP 6500 THERMO Scientific device. The dosing method is described in [24].

The crystallographic properties are observed through the X-ray diffraction (XRD) patterns recorded with a Bruker D8 Twin-Twin powder diffractometer using Cu-Kα radiation. The Scherrer formula (Eq. (1)) is used to determine the diameter of the TiO_2 crystallites, d_{XRD} :

$$d_{XRD} = 0.9\frac{\lambda}{B*\cos(\theta)} \quad (1)$$

where d_{XRD} is the crystallite size (nm), B the peak full width at half maximum after correction of the instrumental broadening (rad), λ the wavelength (nm), and θ the Bragg angle (rad).

Scanning electron microscope (SEM) micrographs arre obtained using a TESCAN Clara microscope under high vacuum at an accelerating voltage of 15 keV. The samples are made conductive by applying a thin layer of gold using a metallizer and finally deposited on a sample port with an adhesive carbon sheet.

The nanoparticle sizes are observed with transmission electron microscopy (TEM FEI TECNAI G2-20 TWIN microscope under an accelerating voltage of 160 kV). The powder sample is dispersed in water using ultrasound, the suspension is then deposited as droplets on a copper grid (Formvar/Carbon 200 Mesh Cu from Agar Scientific) and dried before imaging.

The sample textural properties are characterized by nitrogen adsorption-desorption isotherms in an ASAP 2420 multi-sampler adsorption-desorption volumetric device from Micromeritics. From these isotherms, the microporous volume is calculated using the Dubinin-Radushkevich theory (V_μ). The surface area is evaluated using the Brunauer, Emmett, and Teller theory (S_{BET}).

Optical properties of TiO_2-based materials in the range of 250–750 nm are obtained on a UV 3600 Plus UV–VIS–NIR spectrophotometer from Shimadzu Kyoto Japan. Measurements were performed in diffuse reflectance mode. The baseline was realized using Spectralon as a reference. The spectra are transformed using the Kubelka–Munk function to produce a signal, normalized for comparison

between samples, enabling the band gaps to be calculated. The details of this treatment method are described elsewhere [24].

The zeta potential is measured on the different suspensions of samples in water (1 g/L) with a DelsaNano C device from Beckman Coulter, giving information about colloid stability.

To determine the point of zero charge of a sample (PZC), the method is as follows: 11 glass vials are prepared with 10 mL of milli-Q water. The pH of each of these vials is adjusted with diluted HCl and NaOH solutions to cover a pH range of 2 to 12 with a ΔpH of 1 between each vial. Then, an equal amount of powder sample is placed in each of the vials. The mass of sample to be added must be such that the surface concentration in a vial is 1000 m^2/L, i.e. a specific surface area of 10 m^2 in 10 mL. It is therefore necessary to know the specific surface area of the sample before carrying out this test. Once the sample is suspended in each vial, they are shaken for 1 h on a stirring plate using a magnetic bar. After 1 h of stirring, the pH of each of the vials is measured again and a graph of the final pH versus the initial pH can be drawn. The PZC is given by the pH value at which a plateau appears on the graph [25].

X-ray photoelectron spectra are obtained with a SSI-X-probe (SSX-100/206) spectrometer equipped with a monochromatized microfocused Al X-ray source (1486.6 eV), operating at 10 kV and 20 mA. Samples are placed in the analysis chamber where the residual pressure is about 10^{-6} Pa. The charging effect is adjusted using a flood gun of 8 eV energy and a fine-meshed nickel grid is placed 3 mm above the sample surface. The pass energy is 150 eV and the spot size is 1.4 mm^2. The angle between the normal to the sample surface and the direction of electron collection is 55°. Under these conditions, the mid-height width (FWHM) of the Au 4f7/2 peak photo-peak measured on a standard sample of cleaned gold is about 1.6 eV. The following sequence of spectra is recorded: survey spectrum, C 1s, O 1s, N 1s, Ce 3d and Ti 2p and again C 1s to check the stability of charge compensation with time and absence of degradation of the samples.

The C- (C, H) component of the carbon C 1s peak is fixed at 284.8 eV to calibrate the scale in binding energy. Three other components of the carbon peak (C- (O, N), C = O or O–C–O and O–C=O) have been resolved, notably to determine the amount of oxygen involved in the carbon contamination. Data processing is carried out with the CasaXPS program (Casa Software Ltd, UK). Some spectra are decomposed using the Gaussian and Lorentzian function product model (least squares fitting) after subtraction of a nonlinear Shirley baseline. The molar fractions are calculated using the normalized peak areas based on acquisition parameters and sensitivity factors supplied by the manufacturer.

Electron paramagnetic resonance (EPR) experiments are done at room temperature using a Bruker EMX micro. The modulation frequency is set to 100 kHz and the amplitude modulation is set to 1 Gauss. Resolution is set to 1024 and 4 spectra are acquired for each sample. In a typical experiment, 10 mg of catalyst are put in an EPR tube and put in the EPR cavity.

2.4. Photocatalytic experiments

The photocatalytic properties of the materials are estimated through the degradation of a model pollutant, p-nitrophenol (PNP). For each test, the degradation percentage of PNP is calculated from triplicate experiments.

The experimental set-up is described in a previous study [24]. The PNP degradation is evaluated after 8 h under UV/visible light, thanks to a halogen lamp with a continuous spectrum from 300 to 800 nm (300 W, 220 V) measured with a Mini-Spectrometer TM-UV/vis C10082MD from Hamamatsu. The PNP degradation under visible light is evaluated after 24 h with the same halogen lamp covered by an UV filter that removes wavelengths shorter than 395 nm. The residual concentration of PNP is measured with calibration curves by UV/visible spectroscopy (GENESYS 10S UV–Vis from Thermo Scientific) at 318

nm. For each tested catalyst, three glass test tubes containing the catalytic powder are exposed to light to calculate the PNP degradation, and one is kept in the dark to evaluate PNP adsorption on the sample. One additional flask is exposed to light without catalyst to evaluate PNP natural decomposition under UV/visible or visible light only. In each flask, the initial concentrations of catalyst (if present) and PNP are equal to 1 g/L and 10^{-4} M (pH of 4) respectively. The volume of each flask is 10 mL, and the flasks are agitated by a magnetic stirrer. These tubes are placed in a cylindrical glass reactor with the halogen lamp in the center. The reactor is maintained at constant temperature (20 °C) by a cooling system with recirculating water. The lamp is also cooled by a similar system. Aluminum foil covers the outer wall of the reactor to prevent any interaction with the room lighting. Each catalyst is tested both under UV/visible light and under visible light only.

To assess that complete mineralization of PNP occurs when measuring the degradation with the UV/visible spectroscopy, the samples of the photocatalytic experiments are measured using a total organic carbon analyzer (TOC-L CPN from Shimadzu).

A kinetic study is performed for pure TiO_2, $TiO_2/Ce_{0.06}$ and $TiO_2/Ce_{4.40}$ samples. The kinetic equations are fully described in [26], the equation describing the PNP degradation is:

$$C = C_0 e^{(-k\frac{m}{V_0}t)} \quad (2)$$

Where C is the concentration of the pollutant, C_0 is the initial concentration of the pollutant, k is the kinetic constant, m is the mass of the catalyst, V_0 is the initial solution volume, and t is the time.

By plotting $-\ln(C/C_0)$ as a function of time t, the constant reaction rate k, can be determined.

2.5. Scavenger experiments

Ammonium oxalate (AO, 5 mM), isopropanol (ISOP, 5 mM), and p-benzoquinone (PB, 0.5 mM) are used as, respectively, hole, hydroxyl radical and superoxide scavenger in p-nitrophenol aqueous solution filled with $TiO_2/Ce_{0.06}$ sample to reach a 1 g/L concentration, inspired by [26,27]. Measurements are performed after 8 h (under UV/visible light) or 24 h (under visible light) using a UV/visible spectrophotometer at a wavelength of 318 nm.

2.6. Reuse study

In order to assess the stability of the TiO_2 material photocatalytic activity, recycling experiments are done on pure TiO_2 and $TiO_2/Ce_{0.06}$ samples. These tests consist of doing successive photocatalytic experiments on the samples with centrifugation and washing steps in between, ultrasonic bath is used to resuspend the samples. After 24 h of the photocatalytic test described in section 2.4, the catalysts are recovered by centrifugation (15 000 rpm for 20 min). Then, the same test is executed again for another 24 h. This recycling is made 5 successive times, both under UV/visible light and under visible light, corresponding to 120 h of total irradiation. After the 5 experiments under UV/visible light, the two samples (denoted with "-R" at the end of their name) are characterized by XRD and XPS (as described in section 2.3). $TiO_2/Ce_{0.06}$ sample is also analyzed by ICP after the 5 experiments under UV/visible light.

3. Results and Discussion

3.5. Crystallinity and texture

Figure 1 shows the diffractograms obtained for pure TiO_2 (black) and cerium-doped $TiO_2/Ce_{0.06}$ (red) and $TiO_2/Ce_{4.40}$ (blue) samples respectively, showing the changes due to the extreme cases, namely lowest and highest concentrations doping. Anatase is the only crystalline form present in the pure TiO_2 sample with characteristic peaks at 2θ = 26, 38, 48 and 55 °. The addition of cerium does not alter the appearance of the TiO_2 peaks except for a slight shift to the right for $TiO_2/Ce_{4.40}$. As cerium oxide (Ce_2O_3) concentrations are very low, they are not detected by XRD (see further discussion in XPS section below) [28]. Using the Scherrer formula, the crystallite sizes can be determined, and they are presented in Table 1 for all the photocatalysts. For pure TiO_2, $TiO_2/Ce_{0.06}$ and $TiO_2/Ce_{4.40}$, the sizes are nearly identical at 5.5 nm, 6.1 nm, and 5.3 nm, respectively.

Figure 1 - XRD patterns for pure TiO_2 (black), $TiO_2/Ce_{0.06}$ (red) and $TiO_2/Ce_{4.40}$ (blue) samples. The reference peaks of anatase phase are presented in green.

The nitrogen adsorption/desorption isotherms are presented on Figure 2 for the three same samples as for the XRD. The isotherms show the changes due to the addition of cerium to TiO_2. On Figure 2, the red curve, corresponding to the $TiO_2/Ce_{0.06}$ presents a type IV isotherm, as for pure TiO_2 but with greater porosity, increasing the specific surface area from 79 to 105 m^2/g (Table 1) thanks to the

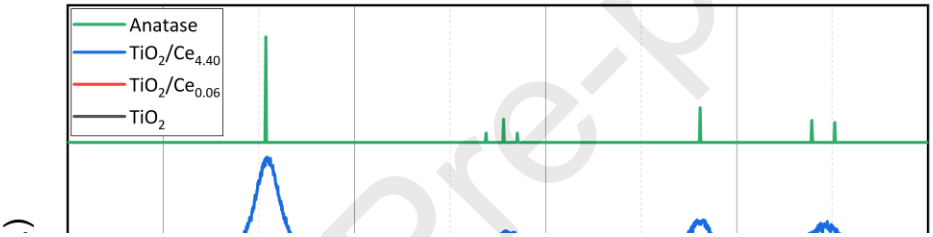

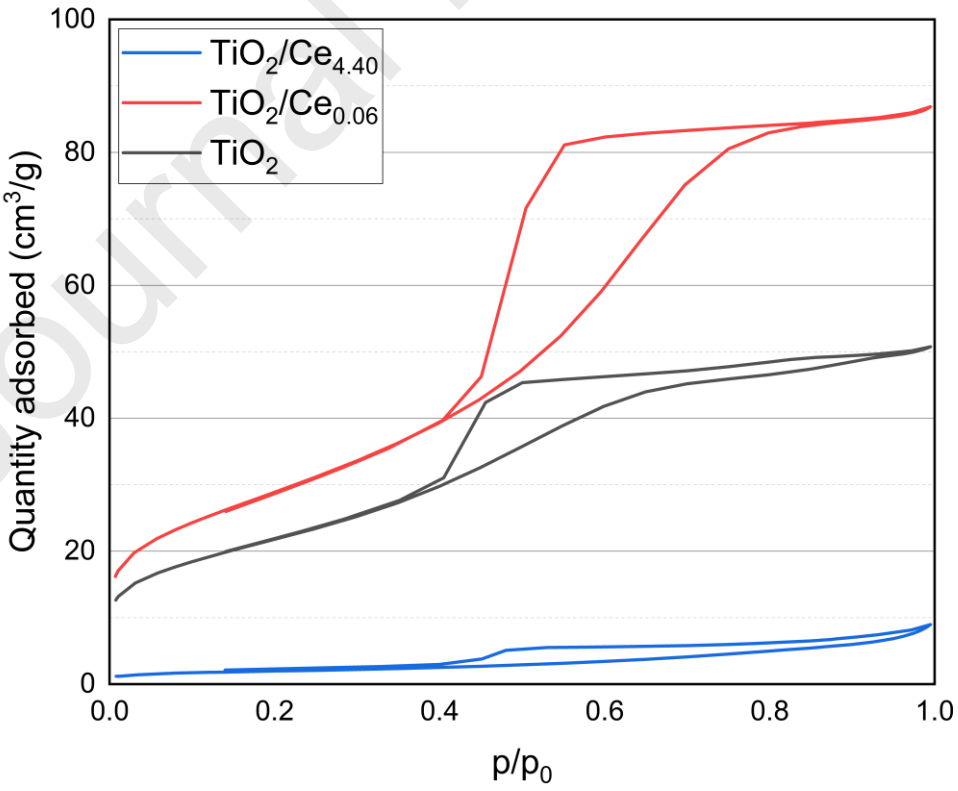

mesopores forming probably between the particles. The $TiO_2/Ce_{4.40}$ sample has very low porosity, which explains its significant reduction in specific surface area to 7 m^2/g. This reduction in specific surface area is probably due to the Ce_2O_3 particles filling the pores between the TiO_2 particles, which is supported by the size of the crystallites obtained by XRD (Table 1), given that these do not change compared with pure TiO_2. This shows that the Ce_2O_3 clogs the pores of the TiO_2 and reduces its specific surface area.

Figure 2 - Nitrogen adsorption/desorption isotherms for pure TiO_2 (black), $TiO_2/Ce_{0.06}$ (red) and $TiO_2/Ce_{4.4}$ (blue) samples.

Table 1: Physico-chemical and optical properties of samples.

Sample	Theoretical Ce amount (mol%)	Actual Ce amount (mol%)	Zeta potential (eV)	S_{BET} (m^2/g)	V_μ (cm^3/g)	d_{XRD} (nm)	$E_{g,indirect}$ (eV)
Pure TiO_2	-	-	8.4	79	0.05	5.5	2.96
$TiO_2/Ce_{0.03}$	0.03	0.03	10.0	105	0.07	6.1	2.96
$TiO_2/Ce_{0.06}$	0.06	0.05	13.1	106	0.07	6.0	2.89
$TiO_2/Ce_{0.30}$	0.3	0.27	10.8	106	0.07	6.1	2.92
$TiO_2/Ce_{0.35}$	0.35	0.38	12.1	105	0.07	6.1	2.91
$TiO_2/Ce_{0.95}$	0.95	1.02	10.5	115	0.07	6.1	2.95
$TiO_2/Ce_{2.30}$	2.30	2.29	12.8	82	0.05	6.1	2.95
$TiO_2/Ce_{4.40}$	4.40	4.39	9.5	7	0.00	5.3	2.86

LoD= limit of detection, S_{BET}= specific surface area measured with BET method, V_μ= microporous volume measured by the Dubinin method, d_{XRD}= crystallite size estimated with the Scherrer formula, $E_{g,indirect}$ = indirect band gap calculated with the Kubelka-Monk function

TEM images of pure TiO_2, $TiO_2/Ce_{0.06}$, and $TiO_2/V_{4.40}$ samples at different magnifications are shown in Figure 3 a, b, and c, representative of the samples. All the samples have a similar aspect corresponding to aggregated TiO_2 nanoparticles that are not clearly defined in the bright-field TEM images, probably because of their low contrast. The similarity between the doped and undoped samples may reflect a good dispersion of the dopants in the TiO_2 matrix. Furthermore, although these particles are not perfectly separated, it is possible to discern a spherical shape for all samples. An estimation of the diameter of all samples is in the same range, around 5-6 nm. This diameter is in the same range of the crystllite size (d_{XRD}, Table 1) estimated from the XRD measurments, assuming that one particle is one crystallite of anatase TiO_2.

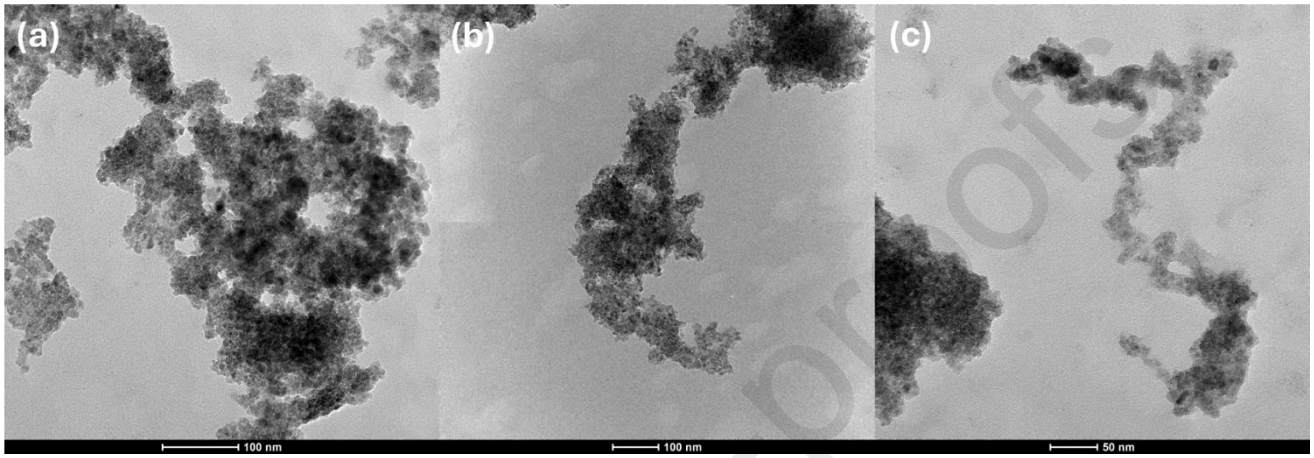

Figure 3 - TEM images of (a) pure TiO_2, (b) $TiO_2/Ce_{0.06}$, and (c) $TiO_2/Ce_{4.40}$ samples.

3.6. Composition

Various techniques, such as ICP, EDX and XPS are used to determine whether the theoretical quantity of cerium is incorporated in the final solids, and the next paragraph is devoted to discussing the results of these characterizations. The ICP results (Table 1) show that all the cerium added based on the theoretical calculations was present in the prepared samples.

In addition, the EDX spectrum for the $TiO_2/Ce_{4.40}$ sample (Figure 4) show the Lα line of cerium emerging at around 5 keV [29]. On Figure 5 (EDX mapping of $TiO_2/Ce_{4.40}$ sample), Ti is shown in blue, O in red and Ce in purple. These data reinforce the results obtained by ICP showing the presence of cerium at a mol% of 3.68, considering the lower precision of EDX [30]. The presence of silicium (in

green) is due to the glass support used for the analysis and the sulfur (in dark blue) comes from the counter ions of the cerium salt used for doping.

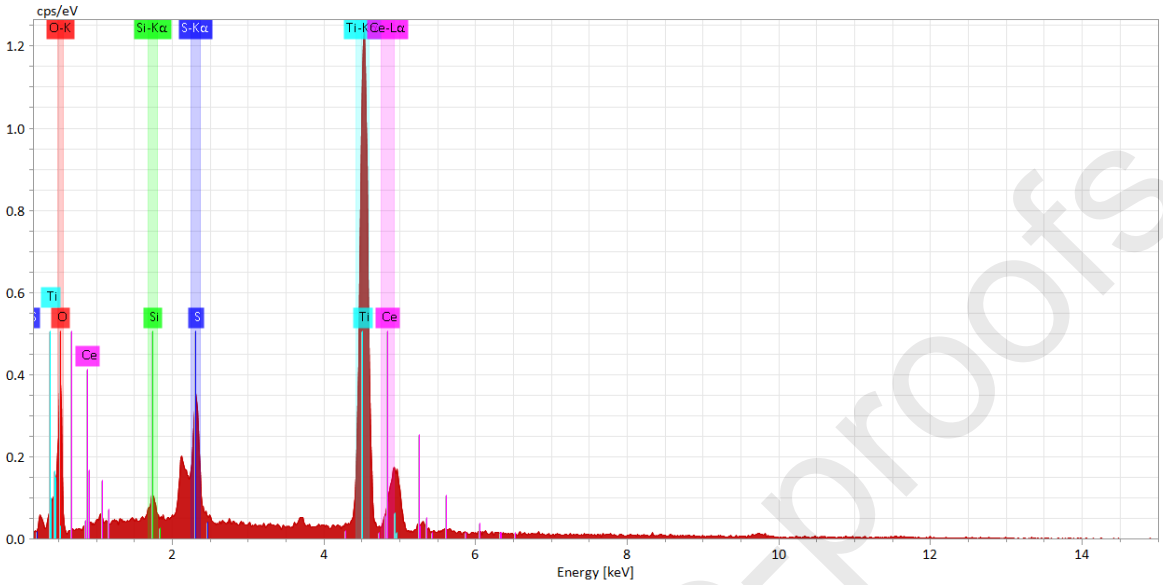

Figure 4 - EDX spectrum of $TiO_2/Ce_{4.40}$ sample.

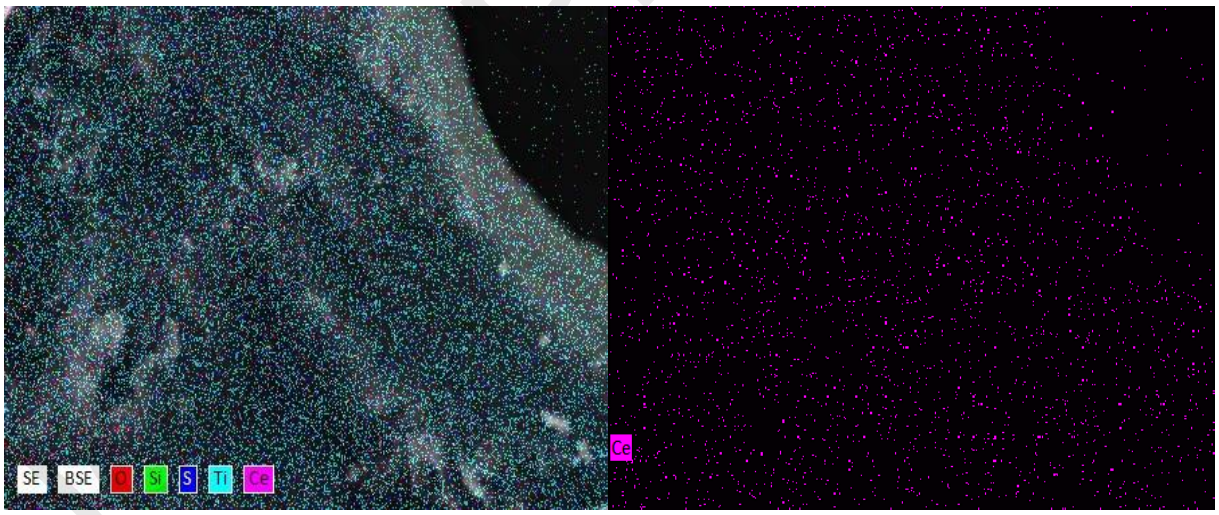

Figure 5 – EDX mapping of $TiO_2/Ce_{4.40}$ sample: on the left oxygen in red, silicium in green, sulfur in dark blue, titanium in blue and finally cerium in purple. On the right the image presenting only the cerium

XPS analysis will reveal the type of bonding and the oxidation state of cerium in the synthesized photocatalysts. Figure 6 shows the various XPS spectra of carbon, oxygen, nitrogen, titanium and cerium for the TiO_2, $TiO_2/Ce_{0.30}$ and $TiO_2/Ce_{4.40}$ samples respectively. Table 2 summarizes the quantification of the main elements detected by XPS (Ce, O, Ti, N and C elements).

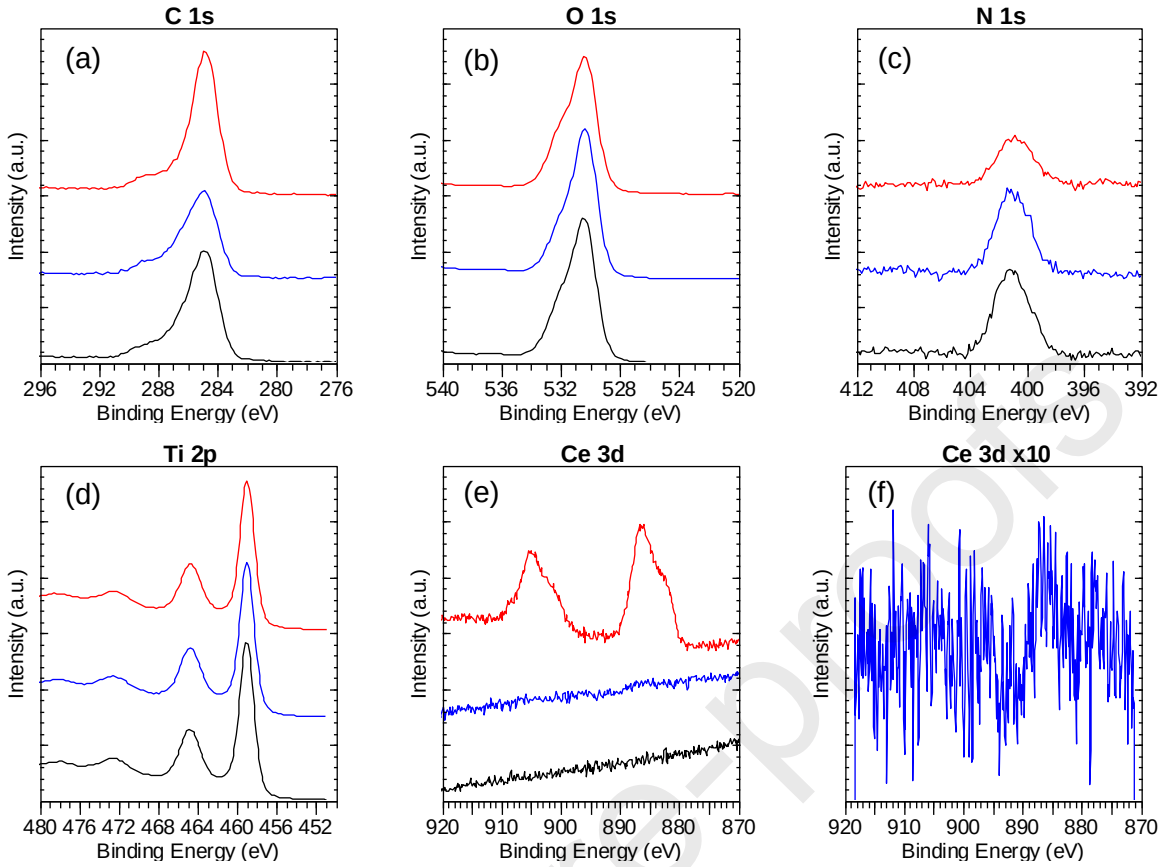

Figure 6 - XPS spectra of pure TiO_2 (black), $TiO_2/Ce_{0.30}$ (blue) and $TiO_2/Ce_{4.40}$ (red) samples: (a) C 1s region, (b) O 1s region, (c) N 1s region, (d) Ti 2p region, (e) Ce 3d region and (f) Ce 3d region 10x zoomed for $TiO_2/Ce_{0.30}$.

Table 2: XPS quantification for Ce, O, Ti, N and C elements.

Sample	Ce (III) (at%)	O (at%)	Ti (at%)	XPS Ce/Ti (mol%)	N (at%)	C (at%)				
						O=C-O	C=O, O-C-O	C-(O,N)	C-(C,H)	C total
Pure TiO_2	-	59.0	18.1	-	1.7	1.0	1.2	3.6	10.9	16.7
$TiO_2/Ce_{0.03}$	<LoD	60.8	19.7	<LoD	1.8	0.9	1.1	4.0	7.7	13.7
$TiO_2/Ce_{0.06}$	<LoD	60.9	19.5	<LoD	1.9	0.9	1.1	3.9	7.9	13.8

$TiO_2/Ce_{0.30}$	0.04	61.2	19.7	0.2	1.6	1.0	1.0	3.5	8.1	13.6
$TiO_2/Ce_{0.35}$	0.05	60.9	19.6	0.25	1.8	0.9	1.2	3.8	8.2	14.1
$TiO_2/Ce_{0.95}$	0.09	59.1	19.3	0.46	1.8	1.1	1.1	4.0	9.4	15.6
$TiO_2/Ce_{2.30}$	0.23	57.7	18.1	1.27	1.6	1.2	1.7	4.7	11.1	18.6
$TiO_2/Ce_{4.40}$	0.63	53.7	16.3	3.86	1.2	1.3	1.4	3.2	17.6	23.5

LoD= limit of detection, XPS Ce/Ti= molar ratio of Ce on Ti measured by XPS.

As for C1s (Figure 6a), it has several components linked to impurities of the C-O, C-(C,H), etc. type that come from the organic products used during synthesis. For the peaks at 285 and 290 eV, each catalyst has a similar percentage of carbon, i.e. around 15% except for $TiO_2/Ce_{4.40}$ which has a higher percentage, i.e. 23%, this higher percentage coming from a larger quantity of C-(C,H).

The O1s spectrum (Figure 6b) shows a peak characteristic of the binding energy of the oxygen atoms bonded to the titanium in TiO_2 at around 530 eV.

The N 1s at 400 and 402 eV on Figure 5c, correspond to impurities presenting N-(CH) and NH^+-(CH) components, respectively [31].

The spectrum of Ti 2p (Figure 6d) consists of two characteristic peaks Ti $2p_{1/2}$ (464 eV) and Ti $2p_{3/2}$ (458 eV), characteristic of Ti(+IV) involved in bonds with oxygen and therefore TiO_2 [32]. There is no difference between the spectra of the three samples. The percentage of titanium is lower for $TiO_2/Ce_{4.40}$ sample, at 16.3 at.% compared with 19.2 at.% for the other photocatalysts. Figure 1 showed a shift in the peaks of the $TiO_2/Ce_{4.40}$ diffractogram, suggesting a disturbance in the crystal lattice caused by the higher quantity of cerium [28]. As cerium is in a +III oxidation state and titanium in a +IV oxidation state, oxygen vacancies are probably created to compensate for the charges [33]. As this type of defect is on the outer surface (outer atomic layer), it is not detected by XPS [34].

Figure 6e shows the XPS spectrum of Ce 3d: two peaks are observed at two different binding energies corresponding to the spin-orbit coupling of the cerium d orbitals: Ce 3d3/2 and Ce 3d5/2 at 905 eV and 885 eV respectively. The shoulders located at energies slightly lower than the main binding energies are due to interactions, after photoemission, of the ejected electron and the remaining core electron, both being unpaired and of opposite spin [35]. Cerium is therefore only present in its +III form and is involved in bonds with oxygen, forming Ce_2O_3. As a reminder, the reagent used is $Ce(SO_4)_2$, which is a source of cerium in a +IV oxidation state. However, the XPS shows the presence of cerium exclusively in its +III oxidation state. This can be explained as follows: the standard potential of the Ce^{4+}/Ce^{3+} pair is around +1.3 and +1.6 V depending on their concentrations [36]. Considering the Nernst equation $E = E_0 - \frac{RT}{nF} \ln(\frac{[Ce+3]}{[Ce+4]})$, the initial concentration of the two species i.e. $[Ce^{+4}] > [Ce^{+3}]$ and the

temperature of the solution (80 °C), the potential tends to increase and Ce +IV is reduced to Ce +III. The other explanation is the reduction of the cerium during the thermal post-treatment at 500 °C.

Finally, a percentage ratio is calculated between cerium and titanium (Ce/Ti) and shown in Table 2. This proportion follows the same trend as the results obtained by ICP but with a lower estimate. This seems logical since ICP analysis is carried out on 1 g of sample, unlike XPS, where the surface area over which the analysis is carried out is much smaller, possibly showing a non-homogeneous dispersion of cerium on a local scale and from the surface to the bulk.

The zeta potential of the suspensions of the photocatalysts in the concentration used during the photocatalytic experiments (1 g/L) is measured and represented in Table 1. All the values are positive (Table 1), as this value is proportional to the surface charge of the particles [37], so the different colloids have a positive surface charge. The zeta potential is related to the stability and so, the dispersion of a suspension [38], the higher the value, the higher the stability and the dispersion. In Table 1, all zeta potentials are in the same range between 8 and 14 eV. The higher value is obtained for $TiO_2/Ce_{0.06}$ sample.

The point of zero charge is estimated (Figure 7) for three samples representative: for pure TiO_2 (black), $TiO_2/Ce_{0.06}$ (red) and $TiO_2/Ce_{2.30}$ (blue) samples. $TiO_2/Ce_{4.40}$ sample is not used for this measurement because its specific surface area (S_{BET}, Table 1) is too low to reach the same conditions of the other samples (1000 m^2 of sample in each vial, see section 2.3 for PZC measurement protocol). The point of zero charge corresponds to the plateau for each sample in Figure 7 and is equal to 5.9, 6.2, and 6.4 for pure TiO_2, $TiO_2/Ce_{0.06}$, and $TiO_2/Ce_{2.30}$ samples, respectively. Similar values are found in literature for TiO_2 samples [39,40]. The introduction of Ce in TiO_2 sample increases slightly the PZC. As the pH of the PNP solution used for the photocatalytic experiments is acid (pH around 4), all samples are positively charged during the PNP degradation.

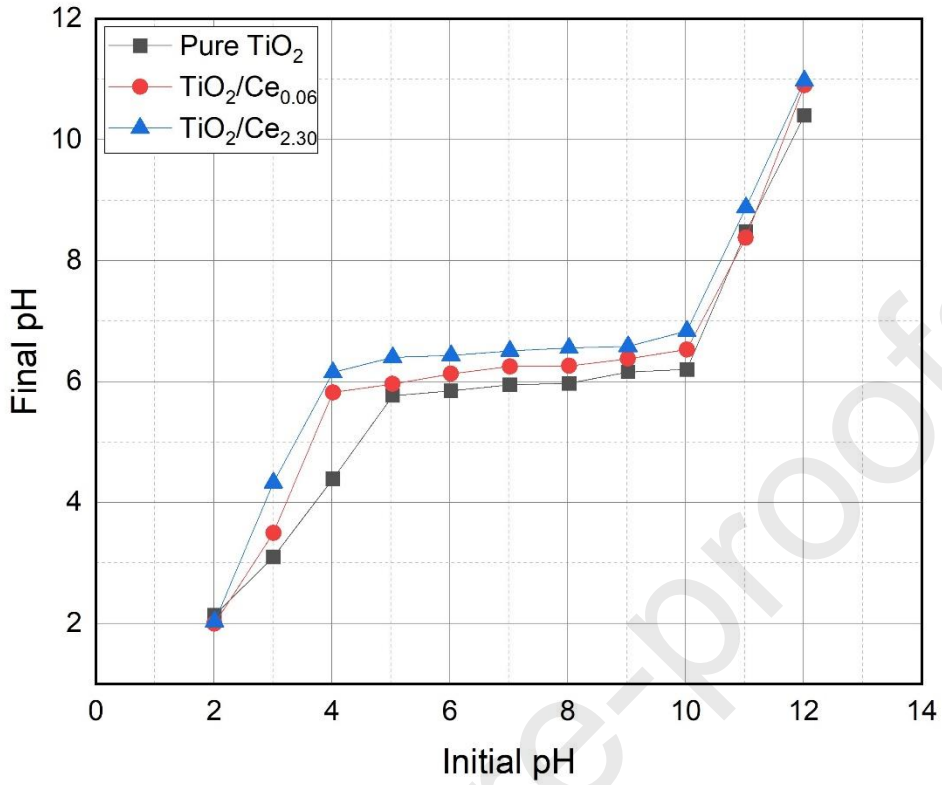

Figure 7 - Final pH vs. initial pH curves for pure TiO_2 (black), $TiO_2/Ce_{0.06}$ (red) and $TiO_2/Ce_{2.30}$ (blue) samples.

3.7. Optical properties & Electron paramagnetic resonance

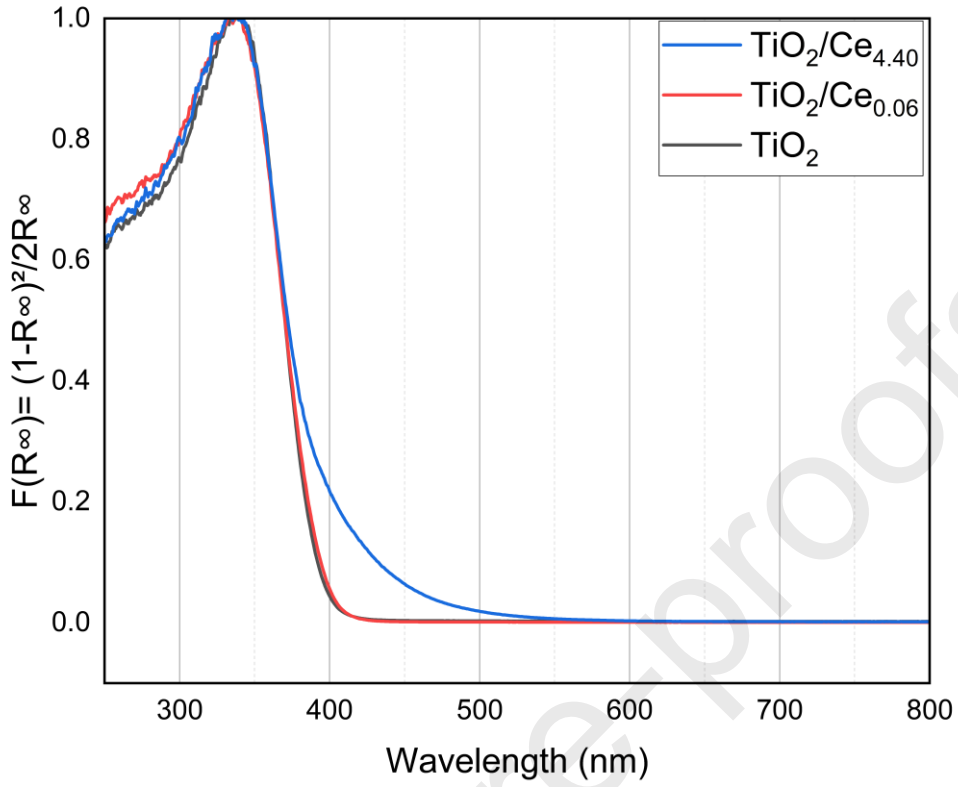

Figure 8- Normalized Kubelka–Munk function $F(R_\infty)$ calculated from DRUS spectra for pure TiO_2 (black), $TiO_2/Ce_{0.06}$ (red) and $TiO_2/Ce_{4.40}$ (blue) samples.

The indirect bandgap values (Table 1 & Figure 8) are similar for all the catalysts, the bandgap value for $TiO_2/Ce_{4.40}$ decreasing slightly compared to that of pure TiO_2, which is consistent with the greater quantity of Ce_2O_3 present in the sample, the latter having a bandgap of 2.4 eV [41] lower than TiO_2 (around 3 eV).

The electron paramagnetic resonance shows no peak between 1000 and 4000 Gauss (graph not shown). This indicates that there is an absence of a deep defect in the bandgap but does not rule out the possible presence of a shallow defect, close to the conduction band and only detectable by low temperature EPR experiment [42].

3.8. Photocatalytic degradation experiments

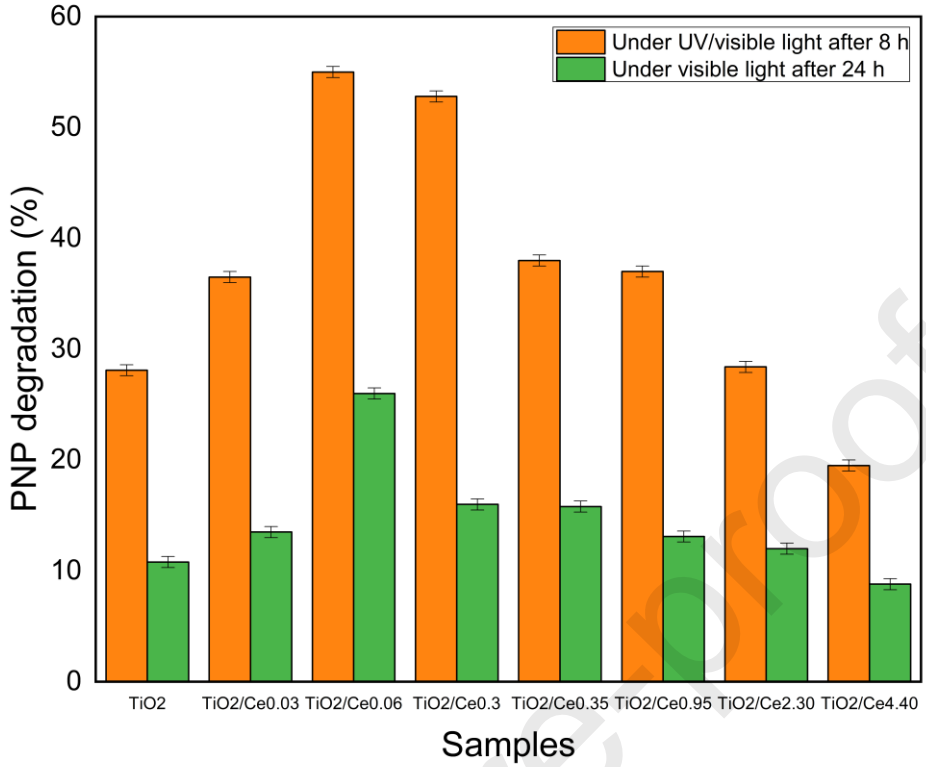

Figure 9 - PNP degradation (%) for all the samples under UV/visible light after 8 h of irradiation (orange) and under visible light after 24 h of irradiation (green).

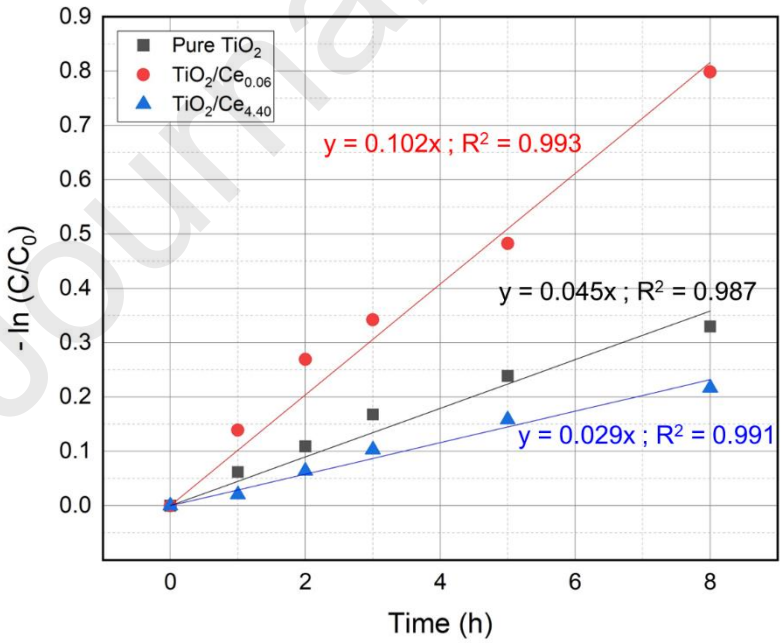

Figure 10 - Experimental determination of kinetic constant of PNP degradation by sampling at 6 different times for pure TiO_2 (black), $TiO_2/Ce_{0.06}$ (red), and $TiO_2/Ce_{4.40}$ (blue) samples.

Results of photocatalytic tests are shown in Figure 9 and the kinetic study of PNP degradation with pure TiO_2, (b) $TiO_2/Ce_{0.06}$, and (c) $TiO_2/Ce_{4.40}$ samples is represented in Figure 10. The photocatalyst showing the greatest PNP degradation rate is $TiO_2/Ce_{0.06}$ with 55% under UV-Visible irradiation after 8h and 26% under visible light (>395nm) after 24h, which is 2 times higher than the pure TiO_2 under UV light and 2.6 times higher under visible light respectively. Figure 9 shows that the quantity of dopant to be added passes through an optimum in degradation efficiency. As the amount of dopant increases, above Ce 0.06 mol%, the photocatalytic activity decreases, both in the UV-Visible and visible range. The evolution between the samples is the same whatever the type of lamp used (UV-visible or visible only). Figure 10 shows that the kinetics of PNP degradation are first order as the fitted curve of $-\ln(C/C_0)$ vs. time being a straight line for the 3 samples, as previously observed in our study [26]. The kinetic constants can be calculated for each sample and are the slopes of the fitted curves in Figure 10. The sample with the highest degradation has the highest kinetic constant ($TiO_2/Ce_{0.06}$ sample, with a kinetic constant of 0.102 h^{-1}, 2.3 times greater than with the pure TiO_2 sample). Several factors influence these results.

Firstly, for $TiO_2/Ce_{0.03}$ to $TiO_2/Ce_{0.95}$ samples, the S_{BET} is around 110 m^2/g, with a crystallite size of 6 nm (Table 1) showing that the only parameter that changes is the amount of cerium. The pore volume is the same for all the catalysts (0.07 cm^3/g) except for the pure TiO_2 (0.05 cm^3/g) and for the $TiO_2/Ce_{4.40}$ (0 cm^3/g) for which the S_{BET} decreases dramatically (7 m^2/g). This underlines that a higher quantity of cerium modifies the photocatalytic activity, showing that an optimum is obtained for the $TiO_2/Ce_{0.06}$ sample. This indicates the tendency of the Ce_2O_3 particles at higher loading to agglomerate and clog the pores between the TiO_2 particles (Figure 2), reducing the number of photocatalytic sites available for PNP degradation [43]. The difference in photocatalytic activity between samples $TiO_2/Ce_{0.06}$ and $TiO_2/Ce_{4.40}$ can therefore be explained by this, but not exclusively.

Since cerium III oxide is a p-type semiconductor with a bandgap of 2.4 eV [44], a synergetic effect can be observed between TiO_2 and Ce_2O_3 by the formation of a heterojunction, making it possible to increase the adsorption spectrum of the photocatalyst and, thanks to the difference in energy between the bandgaps of the two semiconductors, electrons and holes flow from one to the other (Figure 11). At the p-n junction, an electric field is created by the accumulation of charges at the interface of the two semiconductors, accentuating the separation of these charges (Figure 11) [45], a phenomenon observed and reaching its maximum effect for $TiO_2/Ce_{0.06}$.

Concerning the $TiO_2/Ce_{4.40}$ sample, various hypotheses can be formulated as to its lower activity: first, the increased amount of Ce_2O_3, as a p-type semiconductor, may lead to more holes and encourage recombination, as TiO_2 is an n-type semiconductor [46]. Second, as indicated in section 3.1, the amount of titanium decreases while the cerium quantity increases and the diffractogram (Figure 1) shifts to the right, suggesting that a disturbance is introduced into the TiO_2 lattice showing that by switching from Ti +IV to Ce +III on the surface of the catalyst [47], oxygen vacancies are created to compensate for charge losses [47]. Since the EPR spectra do not show any peaks corresponding to oxygen vacancies, this may mean that there are no deep defects in which electrons can be trapped, but it is possible that shallow defects are present. If this is the case, they are only detectable in EPR at low temperatures (under helium) [42]. These shallow defects act as recombination centers, reducing the lifetime of the electron/hole pairs in the Ce_2O_3 hindering the radical production necessary for pollutant degradation [48].

The Ce_2O_3 material is suitable for visible activity (with a bandgap of 2.4 eV [44]) but it is observed that the increase in dopant does not lead to better activity. As mentioned above, it can be linked to the increased amount of Ce_2O_3, as a p-type semiconductor, may lead to more holes and

encourage recombination, as TiO_2 is an n-type semiconductor [46]. This phenomenon has been already noticed in different studies of TiO_2 doping where the dopant has an optimal amount to avoid recombination [24].

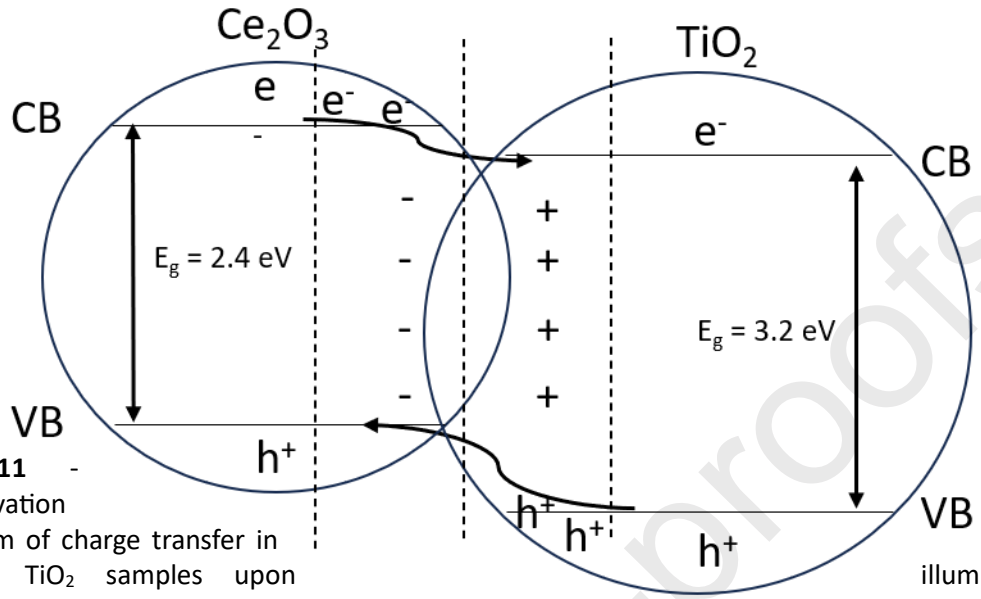

Figure 11 - Possible photoactivation mechanism of charge transfer in the Ce-doped TiO_2 samples upon illumination.

To have information about the species involved in the PNP degradation, scavenger experiments are conducted with $TiO_2/Ce_{0.06}$ sample under UV/visible light after 8 h and under visible after 24 h. The results are presented in Figure 12 with/without the three scavengers, AO, ISOP and PB. The addition of AO as a hole scavenger prevents water from interacting with the holes formed during illumination, resulting in a drastic reduction in the formation of hydroxyl radicals leading to a huge decrease in PNP degradation both under UV/visible and visible light (Figure 12). The trend is very similar when ISOP is used as a hydroxyl radical scavenger, with also a huge decrease in PNP degradation both under UV/visible and visible light. This is consistent with the results obtained with AO, which inhibits the upstream production of hydroxyl radicals by interacting with the holes formed. When PB (superoxide scavenger) is used, a smaller decrease in PNP degradation is obtained, concluding that superoxide plays a lower role in PNP degradation than hydroxyl radicals. These results are consistent with our previous study [26] where hydroxyl radicals and holes are the most important factors for PNP degradation.

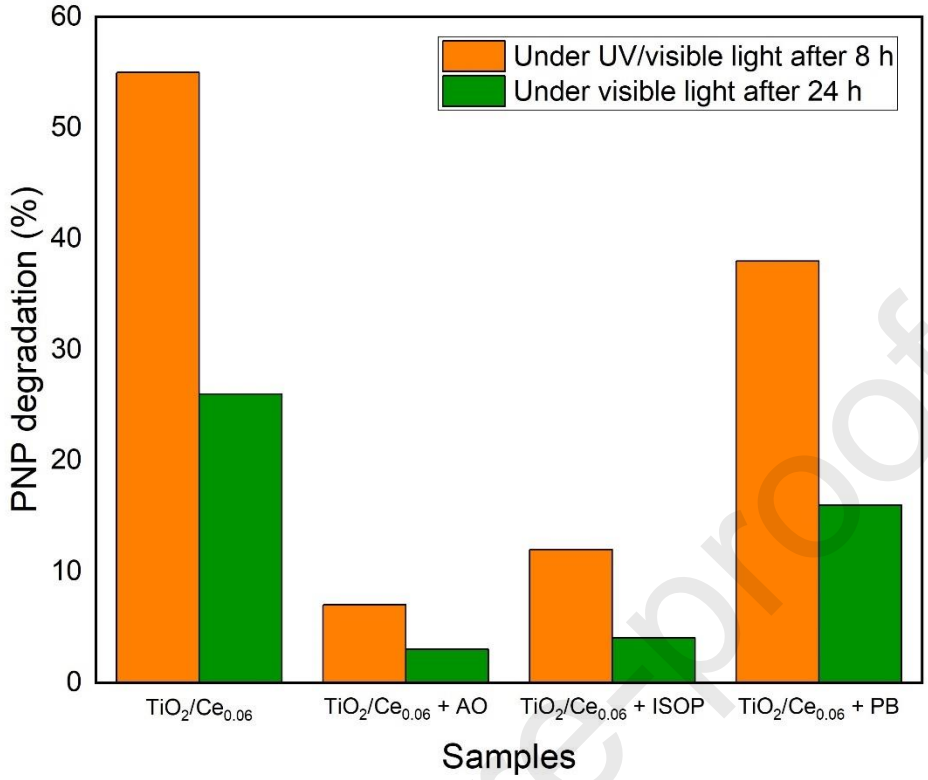

Figure 12 – PNP degradation by the best photocatalyst ($TiO_2/Ce_{0.06}$ sample) with and without scavenger during 8 h under UV/visible light (orange) or during 24 h under visible light (green). AO = ammonium oxalate, ISOP = isopropanol, PB = p-benzoquinone.

TOC measurements are done in parallel with UV/visible spectroscopy to evaluate the mineralization of the model pollutant, the results are presented in Table 3 for the experiments done under UV/visible light. The mineralization follows the measurements made by UV/visible spectroscopy (Table 3 and Figure 9), showing that PNP degradation is a complete degradation of the molecule. Moreover, at the end of the experiment under UV/visible light for the best sample ($TiO_2/Ce_{0.06}$, after 24 h of UV/Visible light illumination) a complete mineralization is obtained with a TOC value of 0 mg of organic carbon per liter. This confirms that the PNP is well mineralized when it is degraded and that no toxic organic by-product remains after the photocatalytic experiments.

Table 3. Total organic carbon (TOC) measurements after photocatalytic experiments (8 h of illumination) compared to the PNP degradation measured by UV/visible spectroscopy.

Photocatalytic experiments after 8 h of illumination under UV/visible light	**Remaining organic carbon by TOC measurements (%)** ± 1	**PNP degradation measured by UV/visible spectroscopy (%)** ± 3	**Remaining PNP from UV/visible spectroscopy (%)** ± 3

Pure TiO_2	72	28	72
$TiO_2/Ce_{0.03}$	64	37	63
$TiO_2/Ce_{0.06}$	44	55	45
$TiO_2/Ce_{0.30}$	48	53	47
$TiO_2/Ce_{0.35}$	61	38	62
$TiO_2/Ce_{0.95}$	62	37	63
$TiO_2/Ce_{2.30}$	74	28	72
$TiO_2/Ce_{4.40}$	81	20	80

The remaining organic carbon was calculated from the TOC measurement before and after the catalytic experiment = $\frac{TOC_{final}}{TOC_{initial}} \times 100$

Concerning the degradation products of PNP during photocatalytic experiments, they are not followed or highlighted in this present study by chromatography but it has been reported in the literature [49,50] that the presence of intermediate species associated with the partial degradation of PNP can be detected by the presence of peaks corresponding to the intermediates (4-nitrocatechol, 1,2,4-benzenetriol, hydroquinone) in the UV/visible spectrum measured between 200-500 nm after several hours under illumination. In the present study, the absence of supplementary peaks in the UV/Vis spectra measured between 200-500 nm is consistent with the complete mineralization of the pollutant and therefore it is concluded that the photocatalysts developed in this study promote the complete mineralization of PNP.

3.9. Reuse study

To assess the stability of the photocatalysts, a reuse study is conducted on pure TiO_2 and $TiO_2/Ce_{0.06}$ samples. Their mean PNP degradations after 5 recycling experiments are shown on Figure 13 both under UV/visible and visible light illumination. Under UV/visible light, it corresponds to the mean value of PNP degradation measured after 8 h of illumination at each cycle while under visible light, it is the mean value measured after 24 h at each cycle. Photoactivity is maintained for both photocatalysts showing their photostability. Moreover, after the 5 recycling experiments under UV/visible light, both the resulting photocatalysts (called pure TiO_2-R and $TiO_2/Ce_{0.06}$-R samples) are characterized by XRD, XPS and ICP (only for $TiO_2/Ce_{0.06}$-R sample). The XRD and XPS results are represented in Figures S1 and S2 in Supplementary Materials and show no modification compared to their initial XRD (Figure 1) and

XPS (Figure 6) results. The ICP measurement confirms the presence of Ce in the same percentage as initially (ie. 0.06 mol%, Table 1). This study confirms the stability of the materials after 120 h of use.

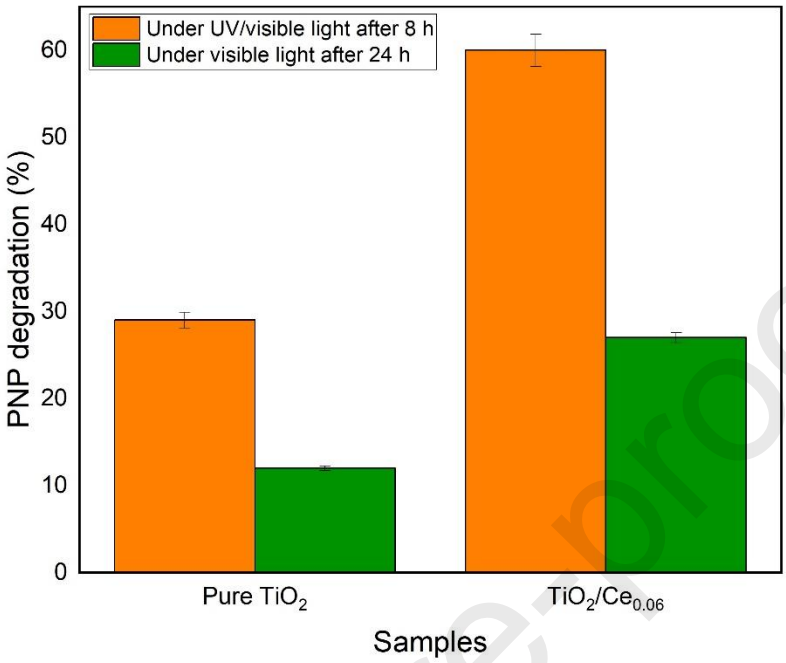

Figure 13 - Mean PNP degradation under UV/visible or visible light for 5 successive photocatalytic tests (120 h of illumination); the mean values correspond to the mean PNP degradation values measured after 8 h of degradation in each of the 5 experiments under UV/visible (orange) or the mean PNP degradation values measured after 24 h of degradation in each of the 5 experiments under visible light (green).

3.10. Comparison with literature

A comparison with similar works from the literature is presented in Table 4, only the best results of each study are summarized. It is difficult to have a direct comparison because, as observed in Table 4, many parameters differ from one study to another as the type of pollutant, its concentration, the lamp used for illumination, the duration of the photocatalytic experiments, the concentration of photocatalysts… Nevertheless, some observations can be drawn.

Dye molecules are often used as model pollutant, with methylene blue the most common [15,51,52]. These molecules are usually more easily degraded by photocatalysis than pharmaceutical or pesticide molecules. The lamp used during the photocatalytic experiments has an important influence on the degradation and the necessary time of exposition to reach it. The more powerful is the lamp, the shorter is the time of exposition to reach higher degradation. In the studies of Table 4, the lamp is usually more powerful than the one used here, leading to faster photocatalytic experiments (usually 2-3 h compared to the 8-24 h in this present study). Concerning the optimal dopant ratio, in the present study, it is 0.06 mol% while it is usually higher in the other studies (between 0.25 to 3 mol%).

To better compare our photocatalysts to reference material, the commercial Evonik P25 TiO_2 was tested in the same conditions as section 2.4 and the results are denoted in Table 4. Under UV light, similar

activity is obtained while under visible light, the beneficial effects of Ce doping are highlighted with a degradation of 25% with the best photocatalyst compared to the 3% reach with P25.

Table 4: Comparison with literature.

References	Photocatalysts	Conditions	Best results
This present work	TiO_2/Ce_2O_3 (0.03 to 4.40 mol%)	PNP (10^{-4} M) 8 h (under UV-visible light, 300-800 nm) Or 24 h (under visible light, 400-800 nm) 1 g/L of photocatalyst	Under UV, 55% with $TiO_2/Ce_{0.06}$ Under visible, 26% with $TiO_2/Ce_{0.06}$
A. Dey et al. 2023 [53]	TiO_2/CeO_2 (0.45 mol%)	Textile effluent 120 min under UV (254 nm) 1.5 g/L of photocatalyst	40% (with 15% of photolysis)
M. Ikram et al. 2023 [51]	TiO_2/Ce^{3+}/Chitosan (2-4 wt% of Ce)	Methylene blue (MB, 10 mg/L) 120 min (Hg lamp, 400-700 nm) 0.33 g/L of photocatalyst	97% (with the 2% sample)
A. Jamil et al. 2024 [52]	TiO_2/Ce^{3+} (3 mol%)	MB (5 ppm) UV lamp (365 nm) Or Sunlight lamp Both for 90 min Photocatalyst concentration not mentioned	Under UV, 50% Under sunlight, 60%
F.B. Li et al. 2005 [54]	TiO_2/Ce^{3+} (0.3 to 2.0 mol%)	2-mercaptobenzothiazole (0.28 mM/L for UV or 0.13 mM/L for visible) UV (365 nm)	100% under UV after 40 min for Ce 1.2 mol% sample 100% under visible after 100 min for

		Or visible (400-800 nm) Both for 120 min 1 g/L of photocatalyst	Ce 0.7 mol% sample
Y. Xie et al. 2003 [55]	TiO_2/Ce^{4+} (3 mol%)	Reactive brilliant red dye (100 mg/L) Visible (400-800 nm) 120 min 1 g/L of photocatalyst	83%
V. Yadav et al. 2023 [56]	TiO_2/Ce (0.1-1 mol%) Mix CeO_2 and Ce^{3+}	Diclofenac (50 ppm) UV (354 nm) 180 min 1 g/L of photocatalyst	90% of degradation after 180 min and Ce 1 mol% sample
J.C. Cano-Franco et al. 2019 [15]	TiO_2/CeO_2 (0.1-5 mol%)	MB (400 ppm Solar light (Xe lamp) 150 min 1 g/L of photocatalyst	98% with Ce 0.25 mol% sample
With commercial Evonik P25, with the condition of the present study	Pure TiO_2	PNP (10^{-4} M) 8 h (under UV-visible light, 300-800 nm) Or 24 h (under visible light, 400-800 nm) 1 g/L of photocatalyst	Under UV, 55% Under visible, 3%

4. Conclusions

In conclusion, TiO_2 was successfully synthesized by a sol-gel method requiring the use of only a few organic compounds (only the titanium precursor). X-ray diffraction showed that only the crystalline anatase phase was formed during synthesis. The addition of cerium sulphate did not alter the diffractograms except for the highest percentage ($TiO_2/Ce_{4.40}$ sample) which provoked a slight shift of

the peaks to the right. The N_2 isotherms showed an increase in the specific surface area for samples up to $TiO_2/Ce_{0.95}$ sample (from 85 to 100 m^2/g) and then a drastic fall to 7 m^2/g for the most heavily doped sample ($TiO_2/Ce_{4.40}$). ICP and EDX confirmed the presence of cerium corresponding to the amount calculated theoretically from introduced amounts. XPS showed that cerium was present in its +III oxidation state, suggesting the presence of Ce_2O_3 in the sample leading to the formation of heterojunction with TiO_2. DRUS then highlighted the presence of Ce_2O_3 by a decrease in bandgap of the composite material, consistent with the fact that pure Ce_2O_3 has a bandgap of 2.4 eV. Photocatalytic PNP degradation tests show that an optimum is obtained for $TiO_2/Ce_{0.06}$ sample, achieving the most significant degradation under UV/visible light with 55% degradation after 8 h under UV-visible (28% for the pure TiO_2) and 26% degradation after 24 h at a wavelength >395 nm (10% for the pure TiO_2). Scavenger experiments showed that the holes and the hydroxyl radicals are the most active species involved in PNP degradation. TOC measurements showed also that a mineralization of PNP happens during the photocatalytic process. Finally, a photoactivation mechanism was proposed, showing the advantage provided by the p-n heterojunction thanks to the formation of Ce_2O_3, creating an electric field likely to maximize the lifetime of the electron-hole pairs and therefore the probability of radical formation leading to the degradation of the pollutant. Some hypotheses, based on the specific surface area and absence of EPR signal, are made to explain the lower efficiency of the most doped sample.

Acknowledgments

Julien G. Mahy thanks the F.R.S.-FNRS for his Postdoctoral Researcher position. The authors thank the CARPORVISU platform of the University of Liège and its manager, Dr. Alexandre Léonard, for the nitrogen adsorption-desorption measurements. The authors thank Martine Dejeneffe for the TEM measurements.

Data availability statement

The raw/processed data required to reproduce these findings can be shared on demand.

Conflict of interest

The authors declare that there is no conflict of interest concerning this work.

Author contributions

Antoine Farcy: investigation, methodology, formal analysis, writing – original draft, writing – review & editing. Maxine Mathy: investigation, formal analysis, writing – review & editing. Louise Lejeune: investigation, formal analysis, writing – review & editing. Pierre Eloy: investigation, formal analysis, writing – review & editing. Sophie Hermans: investigation, formal analysis, writing – review & editing. Patrick Drogui: investigation, formal analysis, writing – review & editing. Julien G. Mahy: conceptualization, methodology, formal analysis, investigation, writing – original draft, writing – review & editing, funding acquisition, supervision.

REFERENCES

[1] R. T., A. Heydari, A. Henni, State of the Art Treatment of Produced Water, in: Water Treatment, InTech, 2013. https://doi.org/10.5772/53478.

[2] G. Crini, E. Lichtfouse, Advantages and disadvantages of techniques used for wastewater treatment, Environ Chem Lett 17 (2019) 145–155. https://doi.org/10.1007/s10311-018-0785-9.

[3] A. Gupta, M.R. Singh, WATER POLLUTION-SOURCES,EFFECTS AND CONTROL, (2016) 1–16. https://www.researchgate.net/publication/321289637.

[4] M.A. Mazhar, N.A. Khan, S. Ahmed, A.H. Khan, A. Hussain, Rahisuddin, F. Changani, M. Yousefi, S. Ahmadi, V. Vambol, Chlorination disinfection by-products in municipal drinking water – A review, J Clean Prod 273 (2020). https://doi.org/10.1016/j.jclepro.2020.123159.

[5] D. Chen, Y. Cheng, N. Zhou, P. Chen, Y. Wang, K. Li, S. Huo, P. Cheng, P. Peng, R. Zhang, L. Wang, H. Liu, Y. Liu, R. Ruan, Photocatalytic degradation of organic pollutants using TiO2-based photocatalysts: A review, J Clean Prod 268 (2020). https://doi.org/10.1016/j.jclepro.2020.121725.

[6] Y. Deng, R. Zhao, Advanced Oxidation Processes (AOPs) in Wastewater Treatment, Curr Pollut Rep 1 (2015) 167–176. https://doi.org/10.1007/s40726-015-0015-z.

[7] A. Babuponnusami, K. Muthukumar, A review on Fenton and improvements to the Fenton process for wastewater treatment, J Environ Chem Eng 2 (2014) 557–572. https://doi.org/10.1016/j.jece.2013.10.011.

[8] A. Khlyustova, N. Sirotkin, T. Kusova, A. Kraev, V. Titov, A. Agafonov, Doped TiO2: The effect of doping elements on photocatalytic activity, Mater Adv 1 (2020) 1193–1201. https://doi.org/10.1039/d0ma00171f.

[9] A. Farcy, S.D. Lambert, D. Poelman, Z. Yang, F. Drault, S. Hermans, P. Drogui, B. Heinrichs, C. Malherbe, G. Eppe, A. Verdin, J.G. Mahy, Influence of crystallographic facet orientations of sol-gel ZnO on the photocatalytic degradation of p-nitrophenol in water, J Solgel Sci Technol (2024). https://doi.org/10.1007/s10971-023-06301-9.

[10] J.G. Mahy, C.A. Paez, C. Carcel, C. Bied, A.S. Tatton, C. Damblon, B. Heinrichs, M. Wong Chi Man, S.D. Lambert, Porphyrin-based hybrid silica-titania as a visible-light photocatalyst, J Photochem Photobiol A Chem 373 (2019) 66–76. https://doi.org/10.1016/j.jphotochem.2019.01.001.

[11] S. Lettieri, M. Pavone, A. Fioravanti, L.S. Amato, P. Maddalena, Charge carrier processes and optical properties in TiO2 and TiO2-based heterojunction photocatalysts: A review, Materials 14 (2021). https://doi.org/10.3390/ma14071645.

[12] J.J. Reinosa, C.M.Á. Docio, V.Z. Ramírez, J.F.F. Lozano, Hierarchical nano ZnO-micro TiO2 composites: High UV protection yield lowering photodegradation in sunscreens, Ceram Int 44 (2018) 2827–2834. https://doi.org/10.1016/j.ceramint.2017.11.028.

[13] J.G. Mahy, S.D. Lambert, R.G. Tilkin, C. Wolfs, D. Poelman, F. Devred, E.M. Gaigneaux, S. Douven, Ambient temperature ZrO2-doped TiO2 crystalline photocatalysts: Highly efficient powders and films for water depollution, Mater Today Energy 13 (2019) 312–322. https://doi.org/10.1016/j.mtener.2019.06.010.

[14] Q. Tian, W. Wei, J. Dai, Q. Sun, J. Zhuang, Y. Zheng, P. Liu, M. Fan, L. Chen, Porous core-shell TixSn1-xO2 solid solutions with broad-light response: One-pot synthesis and ultrahigh photooxidation performance, Appl Catal B 244 (2019) 45–55. https://doi.org/10.1016/j.apcatb.2018.11.045.

[15] J.C. Cano-Franco, M. Álvarez-Láinez, Effect of CeO2 content in morphology and optoelectronic properties of TiO2-CeO2 nanoparticles in visible light organic

degradation, Mater Sci Semicond Process 90 (2019) 190–197. https://doi.org/10.1016/j.mssp.2018.10.017.

[16] A. Jamil, T. Sawaira, A. Ali, M. Awais, A. Habib, T. Hussain, A. Sharif, N. Iqbal, A. Afzal, Ce-TiO2 nanoparticles with surface-confined Ce3+/Ce4+ redox pairs for rapid sunlight-driven elimination of organic contaminants from water, Environ Nanotechnol Monit Manag 21 (2024). https://doi.org/10.1016/j.enmm.2024.100946.

[17] F.Z. Janani, H. Khiar, N. Taoufik, A. Elhalil, M. Sadiq, A. V. Puga, S. Mansouri, N. Barka, ZnO–Al2O3–CeO2–Ce2O3 mixed metal oxides as a promising photocatalyst for methyl orange photocatalytic degradation, Mater Today Chem 21 (2021). https://doi.org/10.1016/j.mtchem.2021.100495.

[18] F.B. Li, X.Z. Li, M.F. Hou, K.W. Cheah, W.C.H. Choy, Enhanced photocatalytic activity of Ce3+-TiO2 for 2-mercaptobenzothiazole degradation in aqueous suspension for odour control, Appl Catal A Gen 285 (2005) 181–189. https://doi.org/10.1016/j.apcata.2005.02.025.

[19] Y.Y. Qi, Z.W. Niu, C. Cheng, Y. Cheng, Structural and elastic properties of Ce2O3 under pressure from LDA+U method, Front Phys (Beijing) 8 (2013) 405–411. https://doi.org/10.1007/s11467-013-0331-y.

[20] J.T. Dahle, Y. Arai, Environmental geochemistry of cerium: Applications and toxicology of cerium oxide nanoparticles, Int J Environ Res Public Health 12 (2015) 1253–1278. https://doi.org/10.3390/ijerph120201253.

[21] E. Casals, M. Zeng, M. Parra-Robert, G. Fernández-Varo, M. Morales-Ruiz, W. Jiménez, V. Puntes, G. Casals, Cerium Oxide Nanoparticles: Advances in Biodistribution, Toxicity, and Preclinical Exploration, Small 16 (2020). https://doi.org/10.1002/smll.201907322.

[22] S. Pooyan spooyan, Sol-gel process and its application in Nanotechnology, Journal of Polymer Engineering and Technology 13 (2005) 38–41. http://polymer.aut.ac.ir/.

[23] N. Kimura, W. Kitagawa, Y. Kamagata, Biodegradation of nitrophenol compounds, Environmental Science and Engineering (Subseries: Environmental Science) 112 (2014). https://doi.org/10.1007/978-3-319-01083-0_1.

[24] J.G. Mahy, S.D. Lambert, G.L.M. Léonard, A. Zubiaur, P.Y. Olu, A. Mahmoud, F. Boschini, B. Heinrichs, Towards a large scale aqueous sol-gel synthesis of doped TiO2: Study of various metallic dopings for the photocatalytic degradation of p-nitrophenol, J Photochem Photobiol A Chem 329 (2016) 189–202. https://doi.org/10.1016/j.jphotochem.2016.06.029.

[25] S. Lambert, N. Job, L. D'Souza, M.F.R. Pereira, R. Pirard, B. Heinrichs, J.L. Figueiredo, J.P. Pirard, J.R. Regalbuto, Synthesis of very highly dispersed platinum catalysts supported on carbon xerogels by the strong electrostatic adsorption method, J Catal 261 (2009) 23–33. https://doi.org/10.1016/j.jcat.2008.10.014.

[26] A. Farcy, J.G. Mahy, C. Alié, J. Caucheteux, D. Poelman, Z. Yang, P. Eloy, N. Body, S. Hermans, B. Heinrichs, S.D. Lambert, Kinetic study of p-nitrophenol degradation with zinc oxide nanoparticles prepared by sol–gel methods, J Photochem Photobiol A Chem 456 (2024). https://doi.org/10.1016/j.jphotochem.2024.115804.

[27] N.A. Ramos-Delgado, D.A. Pino-Sandoval, K. López-Velázquez, C. Englezos, M. Villanueva-Rodríguez, M.A. Gracia-Pinilla, N.D. Boscher, H. J.G.E. Gardeniers, A. Susarrey-Arce, Acetaminophen oxidation under solar light using Fe-BiOBr as a mild Photo-Fenton catalyst, J Photochem Photobiol A Chem 446 (2024). https://doi.org/10.1016/j.jphotochem.2023.115124.

[28] A.A. Flores-Caballero, A. Manzo-Robledo, N. Alonso-Vante, The Cerium/Boron Insertion Impact in Anatase Nano-Structures on the Photo-Electrochemical and Photocatalytic Response, Surfaces 4 (2021) 54–65. https://doi.org/10.3390/surfaces4010008.

[29] M. Breitwieser, C. Klose, A. Hartmann, A. Büchler, M. Klingele, S. Vierrath, R. Zengerle, S. Thiele, Cerium Oxide Decorated Polymer Nanofibers as Effective Membrane Reinforcement for Durable, High-Performance Fuel Cells, Adv Energy Mater 7 (2017). https://doi.org/10.1002/aenm.201602100.

[30] I. Michalak, K. Chojnacka, K. Marycz, Using ICP-OES and SEM-EDX in biosorption studies, Microchimica Acta 172 (2011) 65–74. https://doi.org/10.1007/s00604-010-0468-0.

[31] J.G. Mahy, V. Cerfontaine, D. Poelman, F. Devred, E.M. Gaigneaux, B. Heinrichs, S.D. Lambert, Highly efficient low-temperature N-doped TiO2 catalysts for visible light photocatalytic applications, Materials 11 (2018). https://doi.org/10.3390/ma11040584.

[32] J.G. Mahy, S. Douven, J. Hollevoet, N. Body, T. Haynes, S. Hermans, S.D. Lambert, C.A. Paez, Easy stabilization of Evonik Aeroxide P25 colloidal suspension by 4-hydroxybenzoic acid functionalization, Surfaces and Interfaces 27 (2021). https://doi.org/10.1016/j.surfin.2021.101501.

[33] Y. Pooarporn, A. Worayingyong, M. Wörner, P. Songsiriritthigul, A.M. Braun, A comparative study of doped and un-doped sol-gel TiO2 and P25 TiO2 (photo)electrodes, in: Water Science and Technology, 2007: pp. 153–160. https://doi.org/10.2166/wst.2007.400.

[34] D.N.G. Krishna, J. Philip, Review on surface-characterization applications of X-ray photoelectron spectroscopy (XPS): Recent developments and challenges, Applied Surface Science Advances 12 (2022). https://doi.org/10.1016/j.apsadv.2022.100332.

[35] E. Bêche, P. Charvin, D. Perarnau, S. Abanades, G. Flamant, Ce 3d XPS investigation of cerium oxides and mixed cerium oxide (Ce xTiyOz), in: Surface and Interface Analysis, 2008: pp. 264–267. https://doi.org/10.1002/sia.2686.

[36] W. Schmickler, R.R. Nazmutdinov, Q. Wang, W.A. Daoud, Electrochemistry of Ce(IV)/Ce(III) redox couples in mixed solutions for aqueous flow battery: Experimental and molecular modelling study, Electrochim Acta 368 (2021). https://doi.org/10.1016/j.electacta.2020.137601.

[37] F. D'Orlyé, A. Varenne, T. Georgelin, J.M. Siaugue, B. Teste, S. Descroix, P. Gareil, Charge-based characterization of nanometric cationic bifunctional maghemite/silica core/shell particles by capillary zone electrophoresis, Electrophoresis 30 (2009) 2572–2582. https://doi.org/10.1002/elps.200800835.

[38] J.G. Mahy, F. Deschamps, V. Collard, C. Jérôme, J. Bartlett, S.D. Lambert, B. Heinrichs, Acid acting as redispersing agent to form stable colloids from photoactive

crystalline aqueous sol–gel TiO2 powder, J Solgel Sci Technol 87 (2018) 568–583. https://doi.org/10.1007/s10971-018-4751-6.

[39] M. Kosmulski, Compilation of PZC and IEP of sparingly soluble metal oxides and hydroxides from literature, Adv Colloid Interface Sci 152 (2009) 14–25. https://doi.org/10.1016/j.cis.2009.08.003.

[40] D.L. Liao, G.S. Wu, B.Q. Liao, Zeta potential of shape-controlled TiO2 nanoparticles with surfactants, Colloids Surf A Physicochem Eng Asp 348 (2009) 270–275. https://doi.org/10.1016/j.colsurfa.2009.07.036.

[41] M. Fronzi, A. Soon, B. Delley, E. Traversa, C. Stampfl, Stability and morphology of cerium oxide surfaces in an oxidizing environment: A first-principles investigation, Journal of Chemical Physics 131 (2009). https://doi.org/10.1063/1.3191784.

[42] S.C. Ke, T.C. Wang, M.S. Wong, N.O. Gopal, Low temperature kinetics and energetics of the electron and hole traps in irradiated TiO2 nanoparticles as revealed by EPR spectroscopy, Journal of Physical Chemistry B 110 (2006) 11628–11634. https://doi.org/10.1021/jp0612578.

[43] D.S. Kim, S.J. Han, S.Y. Kwak, Synthesis and photocatalytic activity of mesoporous TiO2 with the surface area, crystallite size, and pore size, J Colloid Interface Sci 316 (2007) 85–91. https://doi.org/10.1016/j.jcis.2007.07.037.

[44] M. Fronzi, A. Soon, B. Delley, E. Traversa, C. Stampfl, Stability and morphology of cerium oxide surfaces in an oxidizing environment: A first-principles investigation, Journal of Chemical Physics 131 (2009). https://doi.org/10.1063/1.3191784.

[45] G.M. Tomboc, B.T. Gadisa, J. Joo, H. Kim, K. Lee, Hollow Structured Metal Sulfides for Photocatalytic Hydrogen Generation, ChemNanoMat 6 (2020) 850–869. https://doi.org/10.1002/cnma.202000125.

[46] H. Wu, S. Meng, J. Zhang, X. Zheng, Y.X. Wang, S. Chen, G. Qi, X. Fu, Construction of two-dimensionally relative p-n heterojunction for efficient photocatalytic redox reactions under visible light, Appl Surf Sci 505 (2020). https://doi.org/10.1016/j.apsusc.2019.144638.

[47] M. Ghorbanloo, A.A. Nada, H.H. El-Maghrabi, M.F. Bekheet, W. Riedel, B. Djamel, R. Viter, S. Roualdes, F.S. Soliman, Y.M. Moustafa, P. Miele, M. Bechelany, Superior efficiency of BN/Ce2O3/TiO2 nanofibers for photocatalytic hydrogen generation reactions, Appl Surf Sci 594 (2022). https://doi.org/10.1016/j.apsusc.2022.153438.

[48] R. Qian, H. Zong, J. Schneider, G. Zhou, T. Zhao, Y. Li, J. Yang, D.W. Bahnemann, J.H. Pan, Charge carrier trapping, recombination and transfer during TiO2 photocatalysis: An overview, Catal Today 335 (2019) 78–90. https://doi.org/10.1016/j.cattod.2018.10.053.

[49] A. Di Paola, V. Augugliaro, L. Palmisano, G. Pantaleo, E. Savinov, Heterogeneous photocatalytic degradation of nitrophenols, 155 (2003) 207–214.

[50] V. Augugliaro, L. Palmisano*, M. Schiavello, A. Sclafani, L. Marchese, G. Martra, F. Miano, Photocatalytic degradation of nitrophenols in aqueous titanium dioxide dispersion, Appl Catal 69 (1991) 323–340. https://doi.org/http://dx.doi.org/10.1016/S0166-9834(00)83310-2.

[51] M. Ikram, R. Raees, A. Haider, A. Ul-Hamid, J. Haider, I. Shahzadi, W. Nabgan, S. Goumri-Said, M.B. Kanoun, S. Ali, Enhanced photocatalytic and antibacterial activity of TiO2 Quantum dots doped with Cerium/Chitosan for Environmental Remediation: Experimental and theoretical approaches, Mater Chem Phys 297 (2023). https://doi.org/10.1016/j.matchemphys.2023.127462.

[52] A. Jamil, T. Sawaira, A. Ali, M. Awais, A. Habib, T. Hussain, A. Sharif, N. Iqbal, A. Afzal, Ce-TiO2 nanoparticles with surface-confined Ce3+/Ce4+ redox pairs for rapid sunlight-driven elimination of organic contaminants from water, Environ Nanotechnol Monit Manag 21 (2024). https://doi.org/10.1016/j.enmm.2024.100946.

[53] A. Dey, S. Korde, P.R. Gogate, C. Agarkoti, Sonochemical synthesis of Ce-TiO2 nanocatalyst and subsequent application for treatment of real textile industry effluent, Ultrason Sonochem 96 (2023). https://doi.org/10.1016/j.ultsonch.2023.106426.

[54] F.B. Li, X.Z. Li, M.F. Hou, K.W. Cheah, W.C.H. Choy, Enhanced photocatalytic activity of Ce3+-TiO2 for 2-mercaptobenzothiazole degradation in aqueous suspension for odour control, Appl Catal A Gen 285 (2005) 181–189. https://doi.org/10.1016/j.apcata.2005.02.025.

[55] Y. Xie, C. Yuan, Visible-light responsive cerium ion modified titania sol and nanocrystallites for X-3B dye photodegradation, Appl Catal B 46 (2003) 251–259. https://doi.org/10.1016/S0926-3373(03)00211-X.

[56] V. Yadav, H. Sharma, R.K. Singh, A. Kumar, V.K. Saini, Cerium and boron co-doping in TiO2 boosts diclofenac photodegradation, Applied Nanoscience (Switzerland) 13 (2023) 5903–5919. https://doi.org/10.1007/s13204-023-02845-y.

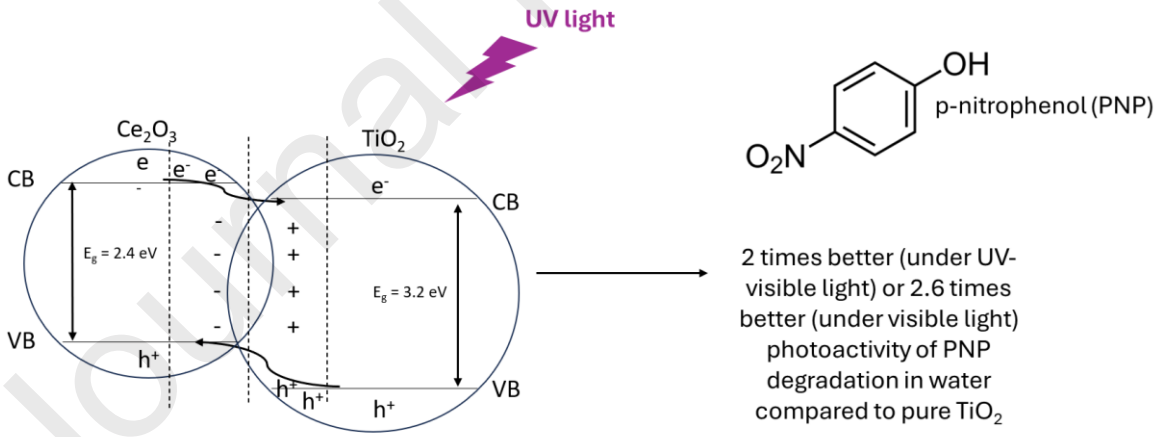

- Sol-gel method is used to synthesize Ce-doped TiO_2, using few organic products.
- The presence of cerium (III) in the sample is confirmed by XPS.
- The addition of cerium leads to the formation of p-n heterojunctions between Ce_2O_3 and TiO_2.
- The photo-efficiency is tested on p-nitrophenol in water under UV or visible light.
- The best dopant amount increases the photocatalytic efficiency by 2 (under UV-visible light) or 2.6 (under visible light).

Author contributions

Antoine Farcy: investigation, methodology, formal analysis, writing – original draft, writing – review & editing. Maxine Mathy: investigation, formal analysis, writing – review & editing. Louise Lejeune: investigation, formal analysis, writing – review & editing. Pierre Eloy: investigation, formal analysis, writing – review & editing. Sophie Hermans: investigation, formal analysis, writing – review & editing. Patrick Drogui: investigation, formal analysis, writing – review & editing. Julien G. Mahy: conceptualization, methodology, formal analysis, investigation, writing – original draft, writing – review & editing, funding acquisition, supervision.